Two-temperature model for ultrafast melting of Au-based bimetallic films interacting with single-pulse femtosecond laser: Theoretical study of damage threshold

Aeaby C. D.* and Aditi Ray
Theoretical Physics Section, Bhabha Atomic Research Centre, Mumbai 400085, India
and Homi Bhabha National Institute, Mumbai 400094, India

(Received 20 October 2022; revised 20 February 2023; accepted 14 April 2023; published 3 May 2023)

Ultrashort-pulse laser excitation and associated thermal damage of single-layer metallic films have been extensively studied both theoretically as well as experimentally. However, study of ultrafast heat transfer mechanism in bimetallic films, a topic of immense current interest for designing next-generation optical components with better thermal resilience, is limited to a low fluence regime. Moreover, available results for damage threshold (DT) of bimetallic films have several ambiguities. The current work is an attempt towards development of comprehensive theory for the DT of Au-based bimetallic films, analyzing its dependence on associated physical parameters and bridging the gap in existing literature. This has been achieved by developing fully implicit two-temperature model-based Python code. Excellent agreement of the predicted temperature profiles with recently reported [E. L. Gurevich, Y. Levy, S. V. Gurevich, and N. M. Bulgakova, Phys. Rev. B **95**, 054305 (2017)] femtosecond laser irradiated Au film validates the code. Subsequently, the code is utilized to investigate the influence of different metallic substrates, M (M = Ni, Cr, Cu) on ultrafast melting damage of Au/M films excited by single-pulse femtosecond laser. Simulations carried out for increasing Au layer thickness revealed a nonmonotonic variation of DT for all substrates. This study also brought out an important observation that for every substrate metal, there exists an optimum Au thickness for maximizing the *incipient* and the *complete melting threshold*. Maximum achievable enhancement for Au/M films over pure Au are found to be 30%, 22%, and 14% with Cu, Ni, and Cr substrates, respectively. The observed distinction in maximum DT among three different Au/M targets is explained by developing appropriate thermophysical models. Finally, an empirical function is proposed here for expressing nonmonotonic variation of two-layer DTs. Very good agreement between the substrate-specific peak positions predicted by the proposed function and effective electron diffusion length arising from thermophysical analysis makes the modeling robust and applicable for a wide range of laser wavelengths as well as arbitrary combinations of bimetallic films.

DOI: 10.1103/PhysRevB.107.195402

I. INTRODUCTION

The physics of ultrashort pulse (USP) laser interaction with matter has been a subject of constant interest due to many prospective and exciting applications in several fields of science and engineering. The minimum heat-affected zone associated with the least collateral damage offered by a femtosecond (fs) laser makes it the most favorable choice among all USP lasers [1]. The availability of powerful fs lasers has reached an advanced stage of scientific, industrial and medical applications. Laser melting and ablation finds its use in nanoparticle generation [2], laser vapor deposition [3], laser-induced breakdown spectroscopy [4], and many other processes. Laser-driven shock provides an excellent platform for characterizing mechanical strength and thermodynamic properties of warm dense matter [5]. With the rapid spread in the domain of applications, the demand for USP lasers is constantly increasing. At this pace, further development towards an increase in average output power may finally be limited by the damage behavior of optical components causing undesirable outcomes and inherent safety aspects questionable.

Fundamental research of laser-induced damage thresholds (LIDTs/DTs) of thin optical films, used as mirrors/gratings in optical/optoelectronic components, is currently of great significance as it is essential for designing high-power laser systems. Although structural and morphological changes cause surface damage as exploited in micromachining and microfabricaton, the prevalent thermal damage mechanism due to irradiation of USP laser is surface melting and ablation. In this context, DTs of various single-layer metal films have been studied extensively both theoretically as well as experimentally. In particular, single and multiple-pulse ablation threshold of Au films have been evaluated experimentally for different pulse-width and wavelength combinations, viz., 600 fs at 1053 nm [6], 200 fs at 400 nm [7,8], 28 fs at 793 nm [9], and many others. All these works confirm that DT is greatly influenced by laser parameters like wavelength, pulse duration, number of pulses, etc. It is also known that damage of Au occurs for much higher incident energy than many common metals.

Under the exotic thermodynamic and optical environments caused by high power lasers, single-layer metal cannot always

*aeabycd@barc.gov.in

 ©2023 American Physical Society

support the required mechanical strength to maintain structural integrity [10]. Multilayer films are now widely used to enhance the application of high-resilient thin films.

Most of the experiments on Au films employ dielectric materials as substrate that does not allow transfer of thermal energy associated with electrons. This renders reduced ablation threshold, thereby facilitating nanoparticle generation. On the contrary, metal substrates that would provide a favorable medium for distributing absorbed energy through electrons, consequently lowering the lattice temperature rise of Au film, have not been studied in great detail. In a major effort, Qiu *et al.* [11,12] explored the energy transfer dynamics in multilayer metals during short-pulse laser heating. Theoretical prediction as well as experimental investigation revealed that Au-coated Cr film can significantly lower the lattice temperature rise in Au layers. Nevertheless, study is restricted to the low fluence regime only. However, this opened the possibility for potential new designs of Au-based optical films for high-power laser applications that would not suffer thermal damage even at very high fluence. New-generation high-power lasers can exploit this fact by employing other Au-coated metals as optical film.

Theoretical [13–16] and experimental [17–19] studies of ultrafast thermalization dynamics of multilayer metal films have been reported more recently. Chen *et al.* [20] estimated the DT of 200 nm equal-width Au/M (M = Cu, Ni, Ag) film for an infrared (IR) laser to show that Ni performs better in enhancing DT. Suslova and Hassanein [21] predicted comparable values of DT for Au/Ni and Au/Cu targets for all Au thicknesses in the range of 25 to 200 nm. Steady decrease of DT with Au thickness as reported in Ref. [21] is the outcome of considering melting of the Au layer only. This approach does not ensure integrity of the double-layer film and extent of thermal damage caused in the second layer while Au is melting. Furthermore, in spite of same laser parameters, there is quantitative disagreement between the DT values between these two works. For example, maximum enhancement for Au/Cu film estimated by Refs. [20] and [21] are 25.6% and 10.5%, respectively. The same for Au/Ni films are 40.7% and 9.5% as reported in these references. Hence, a comprehensive theory on DT enhancement of two-layer film with any arbitrary substrate metal is necessary. Further, in the absence of substantial experimental data, it is very crucial to predict the electron and lattice temperature profiles, basic building blocks of DT, very accurately.

While ablation experiments require relatively higher fluence that favor particle ejection, the reverse is true for investigation of melting damage. An accurate determination of the melting threshold demands high-precision diagnostics for reflectivity measurement. Therefore, theoretical prediction of the melting threshold plays a pivotal role in developing *a priori* knowledge of the fluence range to be scanned.

The simplest theoretical model that describes electron and lattice temperature kinetics in USP laser irradiated metal reasonably well and consequently has been widely employed for five decades is the so-called *two-temperature model* (TTM) proposed by Anisimov *et al.* [22]. Subsequently, this model paved the way to study energy exchange between electrons and phonons and has been successfully utilized to predict the incident fluence for the onset of melting and ablation of various metals [8,23–28].

Despite successful applications and the popularity of TTM, there are several inherent limitations of this model. Some of the limitations can be overcome by incorporating *more detailed physics* for underlying processes, nevertheless maintaining an overall framework provided by TTM. Since its first formulation, various improvements have been proposed in the traditional form of TTM to account for energy transfer by ballistic electrons [29], transient nonthermal electron dynamics immediately after laser excitation [30], an accurate model for temperature-dependent thermophysical properties of metals in terms of electron and lattice ensembles, and spectrotemporal reflectivity and absorption coefficient of metals [31].

Enhanced TTM still falls short of modeling experimentally observed temperature-dependent electron-lattice *e-l* coupling strength accurately. Waldeckar *et al.* calculated the *e-l* coupling strength from computationally intensive method of density functional theory molecular dynamics (MD) simulations [32]. The tight-binding MD approach has also been adopted to calculate the electron and lattice temperature dependence of the *e-l* coupling parameter [33]. Thermal effects of density change, typically ignored in traditional TTM, along with thermal-stress induced material motion has been taken into account by developing continuum formulation of hydrodynamic model coupled with TTM [34–37].

TTM along with its several generalizations serve as a valuable tool in unfolding coupled dynamics of electrons and phonons through appropriate parameters. But availability of these vast set of parameters puts an inherent limitation to the applicability of TTM for arbitrary metals, their alloys, and compounds. *Ab initio* method of *time-dependent Boltzmann equation* [38] improves many of these shortcomings and enables a realistic, parameter-free description of ultrafast phenomena.

Further, kinetic equations of TTM are unable to explain the microscopic mechanism of melting and ablation under the influence of strong lattice overheating. To overcome this limitation of predicting nonequilibrium phase transformation, microstructural changes leading to spallation, laser-induced pressure waves and shock formation, elastic-plastic transition, etc., a *hybrid computational model* that combines the classical MD method with a continuum TTM description is developed. TTM-MD is advantageous as it has shown its potential in providing good insights into the microscopic phenomena of laser melting and disintegration, photomechanical spallation, as well as ablation of many metals [39–45]. The hybrid approach utilizes the advantages of TTM to adequately describe laser energy absorption into an electronic subsystem and its temperature evolution. MD method allows developing the atomistic perspective of lattice heating, provided accurate interatomic potential is specified. The only disadvantage of this method is the requirement of exhaustive computational resources.

While more sophisticated theoretical and numerical approaches are available nowadays, undoubtedly, TTM constitutes the most favorable choice due to its computational simplicity, albeit, it provides sufficient insights on temperature-induced surface modifications and predicts DT quite accurately. In the present paper, we have applied an

improved version of TTM to study the ultrafast melting of bimetallic targets and developed a theoretical perspective of DT enhancement. Our simulation is limited to analytical functions for electron and lattice temperature dependencies of *e-l* coupling factor, heat capacity, and thermal conductivity of electrons. For very high electron temperatures, the thermophysical properties are influenced by thermal excitation of lower band electrons and should ideally come from first-principles electronic-structure calculations [32]. Neglecting these quantum mechanical effects will alter the absolute values of DT, but we believe that the relative comparison of DT will hold good.

The aim of the current paper is to investigate DT of Au film on different metallic substrates, namely, Ni, Cr, and Cu due to thermal excitation of a single-pulse 100 fs laser. Existing literature defines DT as the minimum laser fluence for which the maximum lattice temperature of any surface just reaches its melting point. Experimental determination of DT is based on observed change in reflectivity at melting. Even though reflectivity of metals in their pure phase (solid/liquid) decreases very slowly with temperature, the same reduces drastically at melting [46]. To accommodate this fact, in the current paper we introduce two quantities of interest, i.e., *incipient melting threshold* (IMT) and *complete melting threshold* (CMT).

Following Ref. [20], first we compare IMT of equal-width Au/M (M = Ni, Cr, Cu) films with IMT and CMT of 200 nm pure Au. The paper has been extended to the investigation of Au layer thickness dependence on melting threshold fluence of Au/M target. Our simulation reveals that (i) all three substrate metals improve the IMT/CMT of Au film; (ii) depending on the substrate, there exists an *optimum thickness* of the Au layer that offers maximum enhancement; and (iii) maximum and minimum enhancement occurs for Cu and Cr embedding. Comparative performance of different substrates has been analyzed from a derived set of thermophysical parameters, such as electron diffusion length, electron cooling time, and lattice heating time. Observed difference in maximum DT and optimum Au thickness among three different Au/M targets are shown to be an artifact of thermal effusion of substrate metals and effective electron diffusion length of bimetallic films.

For better interpretation of the observed profile, we have constructed a semiempirical function to express Au thickness dependence of DT fluence applicable for any substrate material. Interestingly, optimum Au thickness predicted by the proposed function shows good agreement with the effective electron diffusion length arising from thermophysical model. Robustness of this function has been demonstrated by applying it to three different substrates and three representative wavelengths.

The current paper is thus an attempt towards modeling nonmonotonic behavior of DT exhibited by Au-based bimetallic films and developing a comprehensive theory of DT enhancement.

The organization of the paper is as follows. In Sec. II, we introduce the simulation essentials including the TTM model (Sec. II A), optical properties (Sec. II B), and thermophysical models (Sec. II C). Code development and its validation are discussed in Sec. III. Section IV is devoted to the main theme, i.e., DT analysis of different two-layer Au/M targets. Thermophysical analysis and semiempirical modeling of the DT profile are discussed in Secs. V and VI, respectively. Important conclusions are summarized in Sec. VII.

II. SIMULATION DETAILS

First, we introduce electron and lattice energy balance equations under the purview of TTM. Thermophysical parameters appearing in TTM equations are also discussed with comparative analysis among four elemental metals used in this paper.

A. Two-temperature model

Interaction between laser and material involves nonequilibrium heat transfer between electrons and lattices and is described through two coupled set of equations for electron temperature T_e and lattice temperature T_l, the so called *two-temperature model* (TTM) [22]. In the present case of heat transport in two-layer film (total thickness L) involving metal I (which is Au for entire study) of thickness L_1 and metal II (Ni/Cr/Cu) of thickness $L_2 = L - L_1$, TTM equations in one spatial dimension can be written as

$$C_e^{\mathrm{I}}\frac{\partial T_e^{\mathrm{I}}}{\partial t} = \frac{\partial}{\partial x}\left(\kappa_e^{\mathrm{I}}\frac{\partial T_e^{\mathrm{I}}}{\partial x}\right) - G^{\mathrm{I}}\left(T_e^{\mathrm{I}} - T_l^{\mathrm{I}}\right) + S, \tag{1a}$$

$$C_l^{\mathrm{I}}\frac{\partial T_l^{\mathrm{I}}}{\partial t} = \frac{\partial}{\partial x}\left(\kappa_l^{\mathrm{I}}\frac{\partial T_l^{\mathrm{I}}}{\partial x}\right) + G^{\mathrm{I}}\left(T_e^{\mathrm{I}} - T_l^{\mathrm{I}}\right), \tag{1b}$$

$$C_e^{\mathrm{II}}\frac{\partial T_e^{\mathrm{II}}}{\partial t} = \frac{\partial}{\partial x}\left(\kappa_e^{\mathrm{II}}\frac{\partial T_e^{\mathrm{II}}}{\partial x}\right) - G^{\mathrm{II}}\left(T_e^{\mathrm{II}} - T_l^{\mathrm{II}}\right), \tag{1c}$$

$$C_l^{\mathrm{II}}\frac{\partial T_l^{\mathrm{II}}}{\partial t} = \frac{\partial}{\partial x}\left(\kappa_l^{\mathrm{II}}\frac{\partial T_l^{\mathrm{II}}}{\partial x}\right) + G^{\mathrm{II}}\left(T_e^{\mathrm{II}} - T_l^{\mathrm{II}}\right). \tag{1d}$$

In the above, $C_e^{\mathrm{I/II}}$ and $C_l^{\mathrm{I/II}}$ are the volumetric heat capacities of electron and lattice pertaining to metals I and II, respectively, whereas $\kappa_e^{\mathrm{I/II}}/\kappa_l^{\mathrm{I/II}}$ are the thermal conductivity of electron/lattice corresponding to two metals. Electron-lattice coupling strengths of metals I and II are denoted as G^{I} and G^{II}, respectively. The laser heat source activated on the front surface of metal I, considered to be Gaussian-shape pulse, is expressed as [20]

$$S = \sqrt{\frac{\beta}{\pi}}\frac{(1-R)I_0}{t_p\delta}\exp\left[-\frac{x}{\delta} - \beta\left(\frac{t-2t_p}{t_p}\right)^2\right]. \tag{2}$$

In Eq. (2), R and δ refer to the reflectivity and optical penetration depth of metal I, t_p is the full-width half-maximum of the linearly polarized laser source, I_0 is the laser fluence and $\beta = 4\ln(2)$. For the present paper, we have used a 100 fs laser. Reflectivity and penetration depth depends on the wavelength (λ) of the laser. Here, we have considered three different wavelengths lying in ultraviolet (UV): $\lambda = 343$ nm, visible: $\lambda = 515$ nm and infrared (IR): $\lambda = 1030$ nm, regime.

Equations (1) are solved with the condition that initially electron and lattice subsystems are at room temperature, i.e.,

$$T_e^{\mathrm{I}}(x,0) = T_l^{\mathrm{I}}(x,0) = T_0, \tag{3a}$$

$$T_e^{\mathrm{II}}(x,0) = T_l^{\mathrm{II}}(x,0) = T_0, \tag{3b}$$

TABLE I. Reflectivity and optical penetration depth (nm) for Au corresponding to three different wavelengths.

λ	IR	Visible	UV
R	0.982	0.595	0.359
δ	12.23	21.0	15.4

with $T_0 = 300$ K. Zero flux boundary conditions are applied at both ends of the double-layer target.

$$\frac{\partial T_e^{\mathrm{I}}(x=0,t)}{\partial x} = \frac{\partial T_e^{\mathrm{II}}(x=L,t)}{\partial x} = 0, \tag{4a}$$

$$\frac{\partial T_l^{\mathrm{I}}(x=0,t)}{\partial x} = \frac{\partial T_l^{\mathrm{II}}(x=L,t)}{\partial x} = 0. \tag{4b}$$

Further, at the interface, i.e., at $x = L_1$, the two layers are in perfect thermal contact, i.e.,

$$T_e^{\mathrm{I}}(x,t) = T_e^{\mathrm{II}}(x,t), \tag{5a}$$

$$T_l^{I}(x,t) = T_l^{\mathrm{II}}(x,t), \tag{5b}$$

$$\kappa_e^{\mathrm{I}} \frac{\partial T_e^{\mathrm{I}}(x,t)}{\partial x} = \kappa_e^{\mathrm{II}} \frac{\partial T_e^{\mathrm{II}}(x,t)}{\partial x}, \tag{5c}$$

$$\kappa_l^{\mathrm{I}} \frac{\partial T_l^{\mathrm{I}}(x,t)}{\partial x} = \kappa_l^{\mathrm{II}} \frac{\partial T_l^{\mathrm{II}}(x,t)}{\partial x}. \tag{5d}$$

B. Optical properties of Au

Since absorption of laser energy depends on reflectivity (R) and optical penetration depths (δ), in Table I we compare these two parameters with respect to Au for IR, visible, and UV radiation as obtained by the modified Drude model [47]. The current paper does not take into account the electron temperature dependence of reflectivity. Nevertheless, our overall conclusion is expected to remain unchanged.

Data shown in Table I communicates that optical absorption reduces from UV to IR regime. Low absorption of optical energy for Au is exploited in high-power IR laser systems as it can withstand very high energy.

C. Thermophysical properties of materials

The main essence of TTM lies in treating electron and lattice subsystems differently as governed by their own thermophysical properties. In the following we describe them separately.

1. Properties of electron subsystem

Electronic heat capacity is assumed to be a linear function of temperature associated with free electrons, i.e.,

$$C_e = \gamma T_e, \quad \gamma = \pi^2 n_e k / 2T_F, \tag{6}$$

where γ is the coefficient of electronic specific heat, n_e is the density of free electrons, and k is the Boltzmann constant. The above relation is applicable as long as $T_e < T_F$, where T_F is the Fermi temperature. We have used experimental values of γ [48] as listed in Table II.

Depending on electron temperature, two different models for thermal conduction of electrons and *e-l* coupling can be found in literature and are shown to have a significant influence on temperature evolution. Model 1 [11] is applicable for relatively low laser excitation where the maximum electron temperature remains negligibly small in comparison to T_F. In this situation, it is reasonable to assume constant value of *e-l* coupling, G_0, and linear dependence of κ_e on T_e [49], i.e., $\kappa_e(T_e) = \kappa_{e0}(T_e/T_l)$. Model 2 applies for higher fluence when thermal excitation of electrons leads to a significant rise in electron temperature (in case of melting/ablation), making complex electron temperature dependence on κ_e and G. For $T_e < 0.2\ T_F$, Wang *et al.* [50] derived an equation by means of electron scattering rates. In our simulation, we have used its modified form, put forward by Christensen *et al.* [51], as given below:

TABLE II. Thermophysical parameters of the metals used in the present paper.

Parameter	Au	Ni	Cr	Cu
κ_{e0} $[W/m/\mathrm{K}]$	318	90	95	401
γ $[J/m^3/\mathrm{K}^2]$	68	1065	194	97
G_0 $[10^{17}W/m^3/\mathrm{K}]$	0.21	3.6	4.2	1.0
A $[10^7/s/\mathrm{K}^2]$	1.18	0.59	7.90	1.28
B $[10^{11}/s/\mathrm{K}]$	1.25	1.4	13.4	1.23
C_l $[10^6 J/m^3/\mathrm{K}]$	2.5	4.1	3.3	3.5
T_M [K]	1337	1728	2180	1358
ΔH_m $[10^9 J/m^3]$	1.22	2.61	2.81	1.83

$$\kappa_e(T_e) = \kappa_{e0} \frac{BT_e}{\left(AT_e^2 + BT_l\right)}. \tag{7}$$

Temperature-dependent *e-l* coupling strength *G(T)* is modeled as [52]

$$G(T) = G_0 \left[\frac{A}{B}(T_e + T_l) + 1\right], \tag{8}$$

where κ_{e0}, G_0 are the corresponding quantities at room temperature; A and B are material dependent constants. In Sec. III, we have explored the implications of using models 1 and 2 in temperature evolution within single-layer Au film. Influence of these two thermophysical models on DT of a 100 nm Au/Cr two-layer target has been investigated in detail by the present authors [53].

2. Properties of lattice subsystem

Lattice heat capacity, C_l is assumed to be constant within the range of electronic temperatures achieved in our study. Numerical values of C_l for four metals used here are given in Table II. In congruence with the fact that energy transport in metals is largely caused by electrons, thermal conductivity of lattice is considered to be 1% of thermal conductivity of electrons ($\kappa_l = 0.01\kappa_e$). Table II also provides melting temperature, T_M, and latent heat of fusion, ΔH_m, for the metals used.

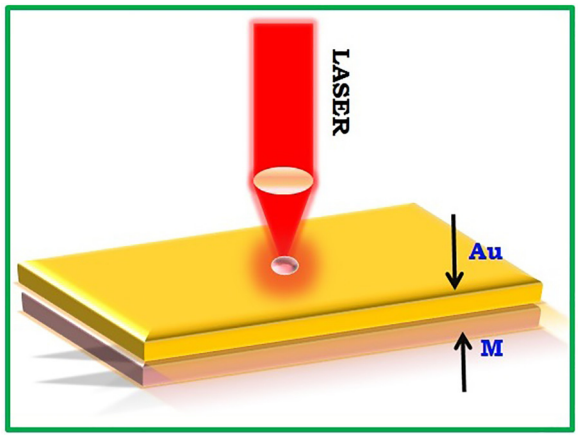

FIG. 1. Schematic diagram of fs laser irradiated two-layer Au/M film. Front layer (Au) of simulation system is in contact with metallic substrate M, where M stands for Ni/Cr/Cu. Melting damage is predicted by analyzing surface temperature of Au and/or M layer.

III. DEVELOPMENT OF TTM CODE AND ITS VALIDATION

For the numerical solution of nonlinear equations [Eqs. (1)], we have developed Python-based TTM code that utilizes fully implicit scheme of the finite difference method [backward time central space-(BTCS)] in one dimension. Like Crank-Nicolson algorithm, this method is also unconditionally stable. The 1D approach makes good approximation as typical spot size of the USP laser is much larger than the depth of the heat affected zone during the interaction time of interest. Implementation of the above equations along with initial and boundary conditions for single material systems is quite straightforward. On the contrary, implementation of the interface condition in the case of heat flow through multimaterial systems demands extra care. There are quite a few different numerical methods for continuity of heat flux at the interface of two dissimilar materials. In our code, we have adopted the *ghost fluid method* [54] with numerical meshes being analogous to fluid elements.

Electron and lattice temperatures are iterated for each time step until the convergence criteria $\Delta T_e/T_{e0} < 10^{-6}$ and $\Delta T_l/T_{l0} < 10^{-5}$ are satisfied. The simulation domain has been divided into 1 nm spatial meshes. Accuracy of the BTCS method has been ensured by choosing adequately small time steps ($\Delta t = 0.1$ fs) so as to maintain truncation error [$\mathcal{O}(\Delta t)$] minimum. Mesh spacing and time step together ensure the stability of numerical solutions. Sensitivity of mesh size on temperature evolution has also been checked before fixing this uniform mesh size for all simulations presented in this paper. The code has been rigorously validated with available results for fs laser absorption and successive heat propagation in single-layer Au film and two-layer Au/Cr system. The schematic diagram of the typical simulation system is displayed in Fig. 1.

First, we validate our code by comparing the time profile of electron and lattice temperatures at the front surface of single-layer Au film as obtained by model 1 with those of Ref. [55] generated for 100 fs laser with peak absorbed fluence of 1100 J/m^2 and $R = 0$. Excellent agreement between the two results (solid lines and symbols) can be observed in Fig. 2(a). The figure also shows the corresponding temperature profiles calculated using model 2 (dashed lines). It can be noticed that for the same fluence, model 2 predicts target melting. Large deviations in temperatures obtained by the two models demonstrate the importance of accurate modeling of κ_e and G.

To validate numerical implementation of heat flow through two dissimilar materials in contact, we have compared our simulation result with analytical solutions of constant heat flux incident on Au/Cr targets [56]. Under this condition, electron and lattice temperature becomes indistinguishable, one talks about material temperature, T, only. Relevant heat transport equations can be obtained by setting $T_e = T_l = T$ and $G = 0$. Adding electron and lattice heat balance equations [Eqs. (1)] for each layer, we arrive at

$$C^i \frac{\partial T^i}{\partial t} = \frac{\partial}{\partial x}\left(\kappa^i \frac{\partial T^i}{\partial x}\right) \; i = \mathrm{I, II}, \tag{9a}$$

$$\kappa^{\mathrm{I}} \frac{\partial T^{\mathrm{I}}}{\partial x} = (1 - R')Q. \tag{9b}$$

In writing Eqs. (9), we have used the notations for bulk properties of individual layers, such as $C = C_e + C_l$ and $\kappa = \kappa_e + \kappa_l$. Following Ref. [56], we take constant heat flux $Q = 10^{14}\ W/m^2$ and absorbance of Au, $(1 - R') = 0.014$. Other boundary conditions are the same as in Sec. II A, except $T_0 = 0$. Figure 2(b) shows three snapshots of spatial distribution of temperature for 200 nm equal-width Au/Cr targets. Solid lines correspond to analytical solutions while symbols represent our simulation results. Excellent agreement between the two validates the thermal conduction model at the contact boundary.

We also validate our code with a standard benchmark problem of 100 nm equal-width Au/Cr target irradiated by 800 nm-100 fs laser [11]. Space-time evolution of electron and lattice temperatures due to incident laser fluence of 500 J/m^2 as obtained with model 1 are presented in Figs. 2(c) and 2(d). The solid and dashed lines refer to temperature transients obtained from our code and those predicted from a *parabolic two-step* model, respectively. Excellent agreement between the two demonstrates the validity and reliability of this code for the present purpose and provides confidence in proceeding further.

Higher lattice temperatures at the Cr layer associated with low temperature rise in Au as seen in Fig. 2(d) is an artifact of much stronger (by one order magnitude) *e-l* coupling strength in Cr. This prompts us to explore the feasibility of enhancing the melting threshold of Au film by embedding with Cr.

IV. DAMAGE THRESHOLD OF TWO-LAYER FILMS

First, we explain the formalism adopted here to quantify the damage. All previous works considered the laser fluence for onset of melting as DT. However, experimental characterization of material temperature is based on observed reflectivity of the irradiated sample. Since reflectivity depends on the melting state of the material, it is prudent to examine the degree of melt when discussing damage. Thus, before proceeding further we introduce two different concepts of DT,

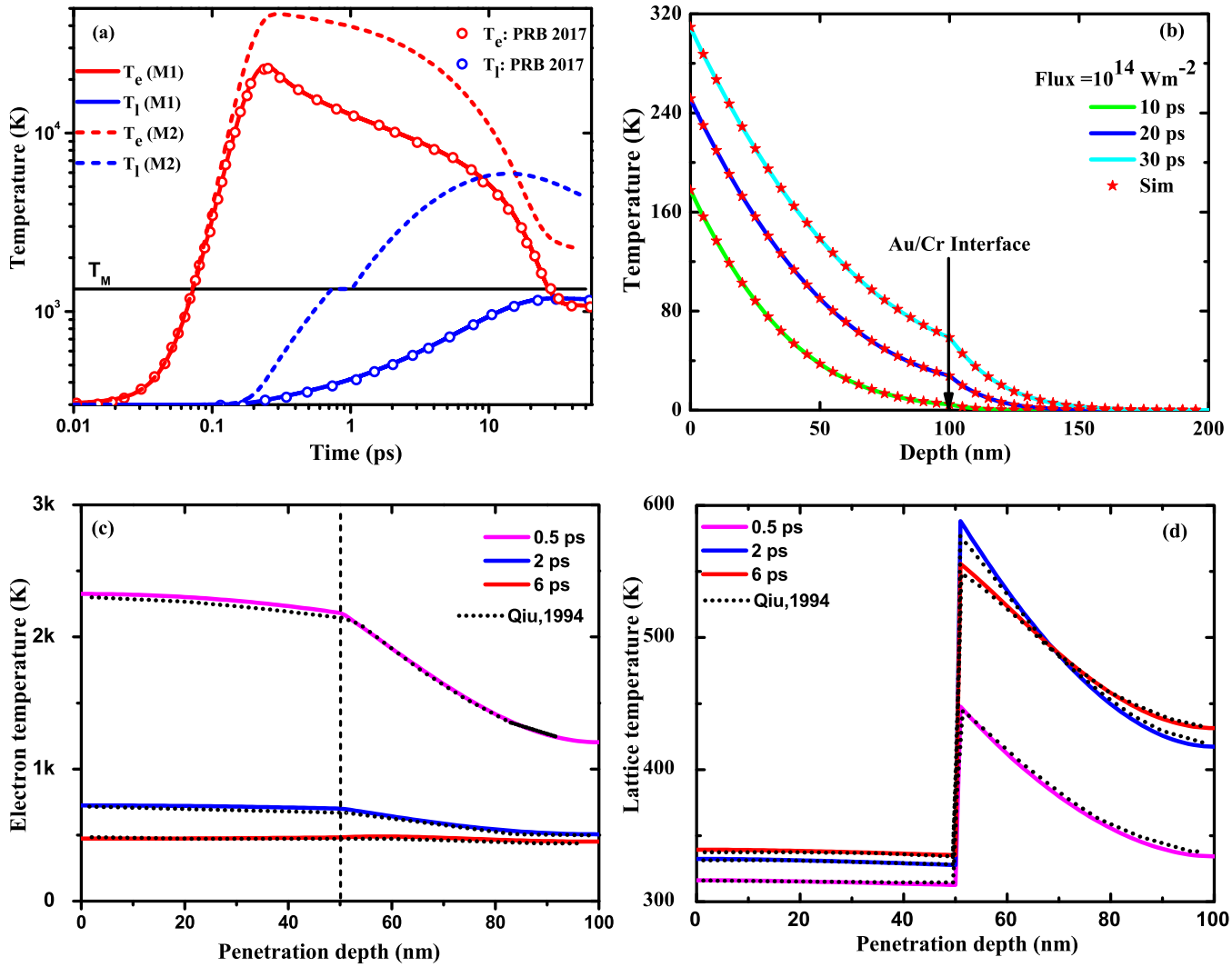

FIG. 2. (a) Time profile of electron (red) and lattice (blue) temperature at front surface of single-layer Au film due to peak absorbed fluence, $I_0 = 1100\ J/m^2$. Solid and dashed lines refer to results of our code with models 1 and 2, respectively; symbols represent results of Ref. [55]. (b) Spatial distribution of temperature within 100 nm Au—in contact with 100 nm Cr for three different times: 10, 20, and 30 ps. Lines and symbols refer to analytical solution as adapted from Ref. [56] and our simulation, respectively. Comparison of spatial profile of (c) electron and (d) lattice temperatures obtained by our code (solid) with Ref. [11] (dashed) for three different times. Last two results are for $I_0 = 500\ J/m^2$.

i.e., IMT or usual DT wherein a tiny spot on the surface of a material just attains T_M and CMT when the spot undergoes complete melting. The measured DT should ideally lie between these two limiting values. Further, keeping the integrity of the composite optical film under thermal stress in mind, IMT/CMT has been assigned when either of the two layers undergoes melting. This would facilitate examining the extent of thermal damage caused in both layers.

CMT has been calculated by incorporating absorption of latent heat corresponding to the layer where melting is initiated as implemented in Ref. [57]. During time evolution, once a numerical mesh(s) of any layer reaches its own T_M, thereafter the laser fluence (I_0) is continued to increase until total lattice energy of that mesh gains its latent heat of fusion. During this process, the temperature of the concerned mesh is maintained constant at T_M. For quantitative description, we introduce *melt fraction* (MF), defined as the ratio of lattice heat absorbed in that mesh to latent heat of fusion calculated when $T_l = T_M$. Thus, CMT fluence will create a spectrum of different MF-valued zones starting from the concerned mesh. Zone depth with varying degrees of MF will eventually be available for ablation. Thus, analysis of CMT would provide a preliminary idea about ablation threshold.

IMT (CMT) of 200 nm pure Au as obtained by our code with the use of model 2 for IR, visible, and UV lasers are 15566 (20075), 756 (990), and 451(588) J/m^2. Our results for absorbed fluence agree with experimental value of about 350 J/m^2 for Au film on fused silica obtained with 200 fs - 400 nm laser [8]. It is worth mentioning here that IMT of 200 nm pure Au irradiated by an IR laser calculated with model 1 is as high as 28550 J/m^2. This overestimation of DT is due to underestimation of peak temperatures in model 1 as observed

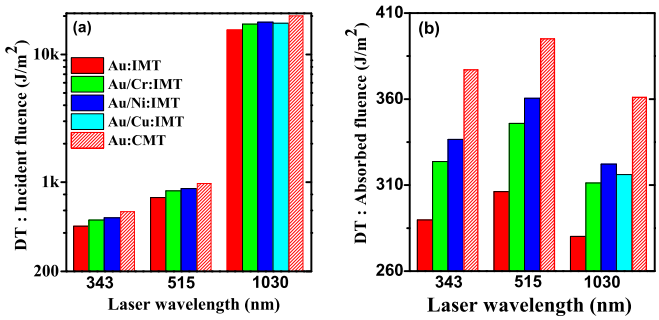

FIG. 3. Comparison of IMT in terms of (a) incident and (b) absorbed fluence of 200 nm single-layer Au (red) with equal-width (100 nm each) Au/Ni (blue), Au/Cr (green) films for three wavelengths and Au/Cu (cyan) for IR laser. Also seen are CMT of single-layer Au film (patterned bars).

in Fig. 2(a) (solid lines). With this observation, hereafter all the results are generated using model 2.

A. DT of equal-width Au/*M* two-layer films

First, we use our code to study the influence of substrate metal on IMT of Au/*M* films when both the layers are of same width. Figure 3 shows minimum incident (a) and absorbed (b) fluence required for incipient melting of equal-width Au/Ni and Au/Cr targets for three different wavelengths corresponding to UV, visible, and IR regimes and Au/Cu target for only the IR laser. For comparison, we have displayed corresponding quantities for pure Au as well. Figure 3(a) conveys that threshold is lowest in the UV regime, marginally higher in the visible regime, and almost one order of magnitude higher in the IR regime. This is in accordance with optical absorptivity of Au at these wavelengths. It is evident that all three substrates offer similar benefits in enhancing melting threshold. Enhancement is clearly visible in the absorbed fluence profile demonstrated in Fig. 3(b). For quantitative comparison offered by different substrates, we define relative enhancement as

$$\Delta F = \frac{(\mathrm{DT}_{\mathrm{Au}/M} - \mathrm{DT}_{\mathrm{Au}})}{\mathrm{DT}_{\mathrm{Au}}} \times 100\%. \tag{10}$$

DT in Eq. (10) refers to IMT/CMT as the case may be. Interestingly, no significant difference in enhancement is observed among the three different wavelengths. For example, ΔF for the Ni substrate is 16.4%, 17.7%, and 15.0% for $\lambda = 343$, 515, and 1030 nm, respectively. Similarly, ΔF for Cr for the same λs are 12.0%, 13%, and 11.1%. With the Cu substrate, enhancement in the IR regime is 12.5%. Maximum enhancement in IMT can be achieved by Ni substrate. Apparently, Cu does not offer any great benefit in this equal-width layer combination. It is worth mentioning here that the reported value of IMT for equal-width Au/Ni and Au/Cu targets are 13830 and 13760 J/m^2 [20] as against 17 900 and 17 560 J/m^2 obtained in our simulation. The reason for this deviation is the reflectivity ($R = 0.974$) and optical penetration depth ($\delta = 13.7$ nm) of Au corresponding to $\lambda = 800$ nm considered in that study. However, the reason for the projected enhancement of 25.6% for Cu and 32.7% for Ni cannot be explained. Interestingly, enhancement realized for these two substrates by our code are comparable with those reported in Ref. [21].

Figure 3(a) also conveys that CMT of 200 nm pure Au are marginally higher than IMT of Au/*M* films.

B. Effect of Au layer thickness on temperature profile of Au/*M* films

Before proceeding for estimating DT of bimetallic films, we investigate the influence of first-layer (Au) thickness, L_1, on electron and lattice temperature profiles of 200-nm Au/*M* films and compare them with pure Au results. Time evolution of T_e and T_l at Au front surface (solid) and two-layer interface (dashed), simulated for IR laser with a fluence of 15566 J/m^2, i.e., IMT of 200 nm pure Au are presented in Fig. 4. The figure demonstrates results for three representative cases with $L_1 = 50$, 100, and 150 nm and the rest Ni/Cr/Cu. After an initial sharp rise T_e, all cases reduce with time. The presence of a second layer accelerates this reduction. Transfer of electron heat energy from the first layer (Au) to the second layer (*M*), as implied by the higher value of peak electron temperature $T_e^{\max}$ at 50 nm Au/150 nm *M* contact surface, is responsible for this. Increase in L_1 also reduces $T_e^{\max}$ at the interface from 5000 K to about 2000 K for all the cases. On the other hand, lowering the thickness of the Au film gradually moderates the lattice temperature of the Au surface at the cost of rising T_l at the interface. Nevertheless, in the case of Ni and Cu, T_l never reaches their corresponding melting temperatures. Lattice temperatures at the Au/Cu interface maintain noticeably low values. Cr, however, undergoes melting for $L_1 = 50$ nm. Figure 4 thus indicates that melting of the Au surface would happen for still higher fluence than IMT of pure Au.

In Fig. 5 (left panels), we compare the temporal profiles of lattice temperature distribution within 200 nm pure Au (topmost), 90 nm Au supported by 110 nm Ni (middle) and 90 nm Au plus 110 nm Cr (bottommost) targets. All cases refer to $I_0 = 990$ J/m^2, which is the CMT of 200 nm Au for $\lambda = 515$ nm.

It can be noticed that lattice temperature distribution for single-layer and two-layer films are significantly different. Film thickness within which melting occurs is referred to as *the melt zone*. A hump in the temperature profile at the Au/*M* interface region and reduction in melt zone in Au film can be easily noticed. Due to higher *e-l* coupling strength than Au, the electron energy couples more effectively to the lattice in Ni and Cr substrates and redistributes the deposited laser energy. This eventually leads to preferential lattice heating in the substrate metals, leading to limited melt-zone depth in Au as compared to bare Au film.

It is also evident from Fig. 5 that at the time of complete melting of the concerned mesh, neighboring meshes also initiate melting. This generates a spectrum of varied MF in the melt zone. Distributions of MF along the target depth at a time when it attains the maximum value in any layer are shown in the right panels of Fig. 5. It can be observed that at CMT of pure Au, the maximum MF attained in Au is 1.0 (100%) with melt-zone depth of 34 nm (topmost). This is similar to the ablation depth of pure Au at its threshold [25,58]. Melt-zone

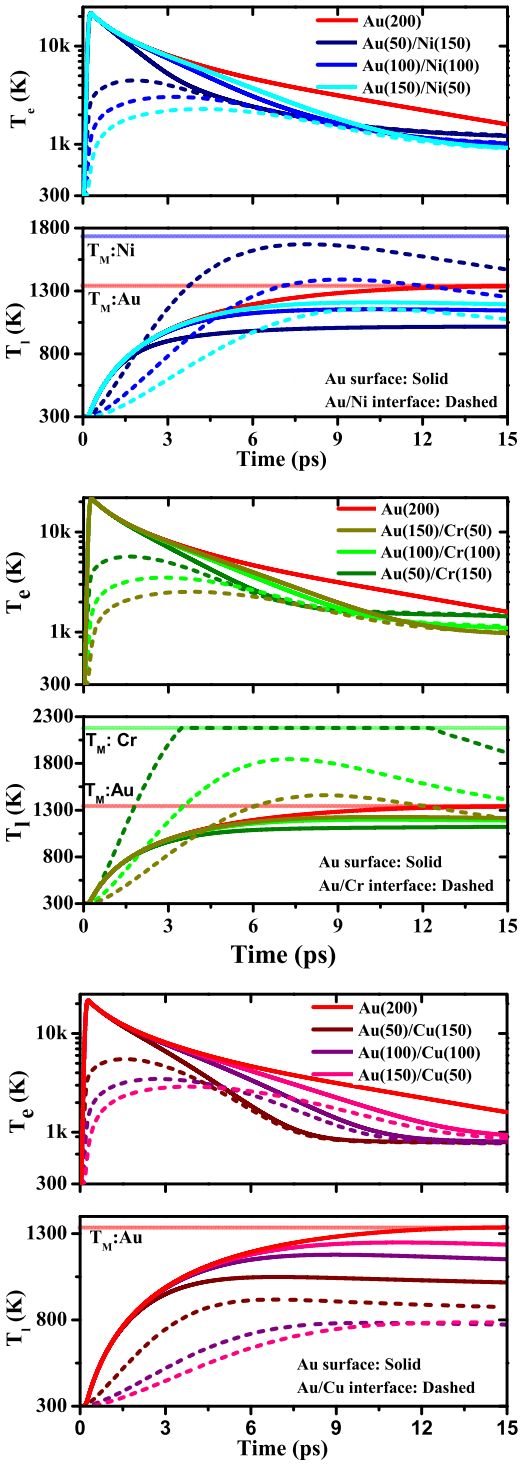

FIG. 4. Time evolution of electron and lattice temperatures for 200 nm Au/Ni (top-most), Au/Cr (middle), and Au/Cu (bottom-most) targets. Solid and dashed lines refer to temperatures at Au front surface and Au/M interface, respectively. Three different Au thicknesses are shown by different shades. All results refer to $I_0 = 15566\ J/m^2$, i.e., IMT of pure Au film.

depth reduces to 12 nm with maximum MF value of 0.32 at the cost of a narrow (4 nm) melt zone within the Ni layer with 28% melting. A similar width (5 nm) melt zone is also generated in Cr but with 64% melting. The melt zone in Au for the Au/Cr case extends to 20 nm with maximum MF of 0.46.

C. Effect of Au layer thickness on DT of Au/M films

To explore the maximum achievable enhancement by any substrate, we have determined two-layer DT by increasing Au layer thickness (L_1) in a systematic manner. Figure 6(a) presents IMT (half-filled circles) and CMT (filled circles) data of Au/Ni (blue), Au/Cr (green), and Au/Cu (purple) targets as obtained by our code for $\lambda = 1030$ nm. The figure conveys that for any Au/M target, the thermal DT initially increases with L_1, reaches a maximum value, and finally reduces on further increase of L_1. The optimum thickness of the Au layer, $L_{\rm opt}$, for which the two-layer target can withstand maximum fluence depends on the substrate material. It is clear that at this wavelength, $L_{\rm opt}$ is lowest for Au/Cu ($\approx$40 nm) and highest for Au/Cr (92 nm), whereas Au/Ni is marginally lower than Au/Cr.

From the data presented in Fig. 6(a), it is also apparent that the maximum and minimum of IMT is achieved by Cu and Cr substrates, respectively. Moreover, for any two-layer film, CMT follows the same profile as IMT. Parallel nature of CMT and IMT profiles is due to absorption of latent heat pertaining to first (for $L_1 > L_{\rm opt}$) and second (for $L_1 < L_{\rm opt}$) layers in raising lattice thermal energy from incipient melting to partial melting of both layers with varied MF, as illustrated in Fig. 5.

Finally, relative enhancements in IMT due to three different metal substrates for few representative Au layer thicknesses, calculated by Eq. (10), are shown in Fig. 6(b). Negative ΔF conveys a lower value of IMT for Au(50)/Cr(150) than IMT of 200 nm Au. Maximum values of ΔF (IMT) are 30% (Cu), 22% (Ni), and 14% (Cr).

It may be noted here that simulation results of Ref. [20] showed the Ni substrate to offer maximum enhancement, while Ref. [21] demonstrated a steady decrease of DT with increasing Au thickness with comparable performance of Ni and Cu substrates. Reference [20] also reported a nonmonotonic profile of DT for the Au/Ni target, but the position of maximum is at $L_{\rm opt} = 125$ nm. Therefore, the current study reveals nonmonotonic behavior of DT exhibited by all three Au/M targets. This prompts us to develop a comprehensive theory that explains this universal feature of peaking in DT at some Au thickness.

Figure 6(c) demonstrates the time of melting of three different Au/M films as a function of increasing Au layer thickness. The data corresponds to melting of either of the two layers at their respective IMT fluence as displayed in Fig. 6(a). It can be noticed that for Au/Cu and Au/Cr targets, melt time (thermalization time) increases with Au layer thickness. For the Au/Ni target, the increase is less significant. From Fig. 4, it can be inferred that thermalization time, $\tau_{\rm th} = \tau_e\tau_l/(\tau_e + \tau_l)$ for 200 nm pure Au is about 15 ps. The corresponding value obtained by using τ_e and τ_l as provided in Table III is 13.3 ps. Much higher value of melt time in pure Au indicates faster melting dynamics for two-layer targets.

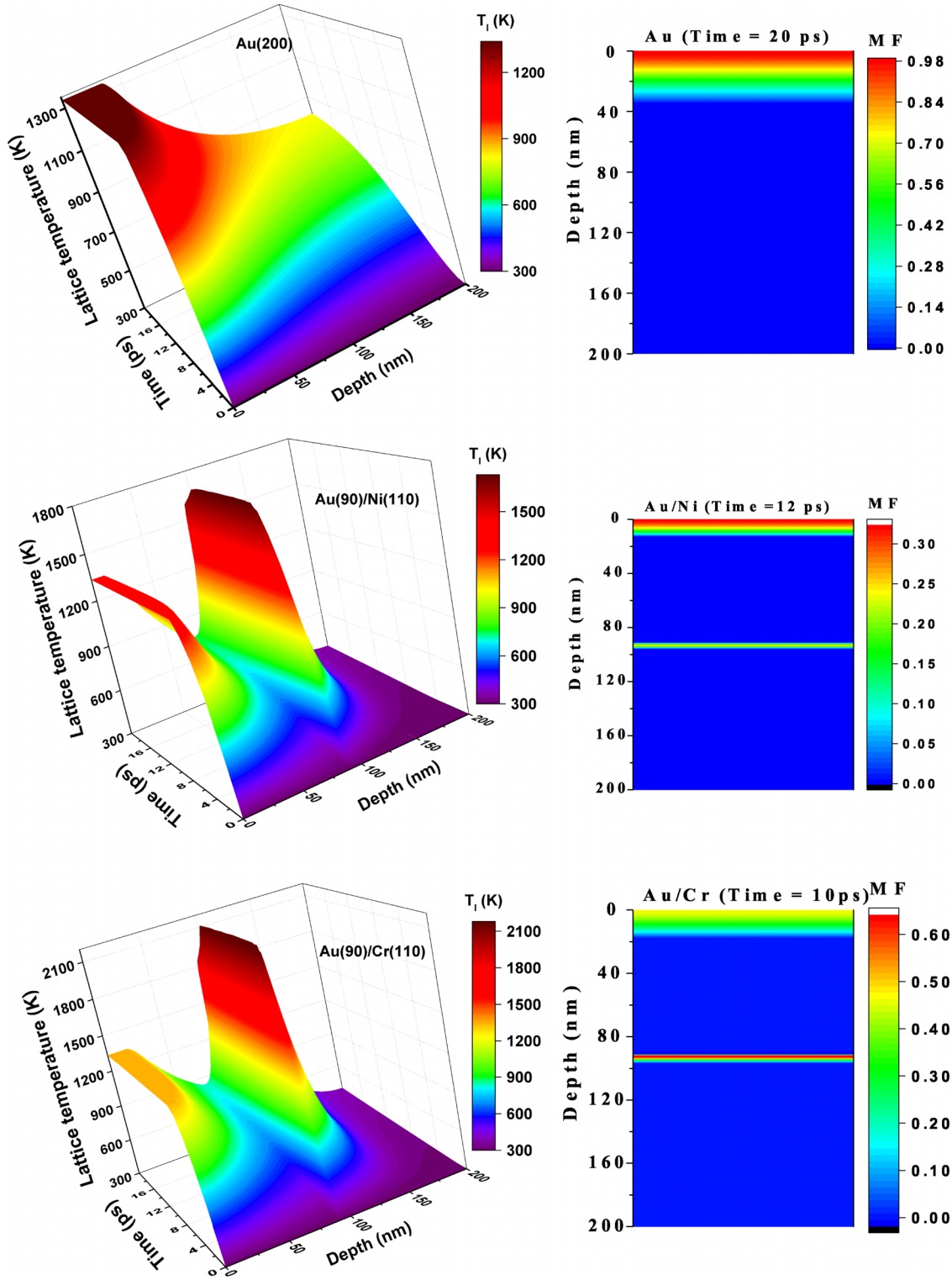

FIG. 5. Left panels: Space-time evolution of lattice temperature in 200 nm films due to laser heating at $I_0 = 990\ J/m^2$, which is CMT of pure Au at $\lambda = 515$ nm. Right panels: Corresponding melting fraction along the target thickness at a time (as indicated) when maximum MF is attained in any layer. Three cases refer to pure Au (top-most), Au(90)/Ni(110) (middle), and Au(90)/Cr(110) (bottommost).

D. Influence of laser wavelength on temperature evolution of Au/*M* films

To elucidate the effect of varied optical absorption in Au corresponding to different wavelength lasers, first we analyze the time evolution of electron temperature at the Au surface. Solid, dashed, and dash-dotted curves of Fig. 7(a) reflect the same for 200 nm targets: Au (red), equal-width Au/Ni (blue), and equal-width Au/Cr (green), for IR, visible, and UV lasers, respectively. Results are generated for CMT

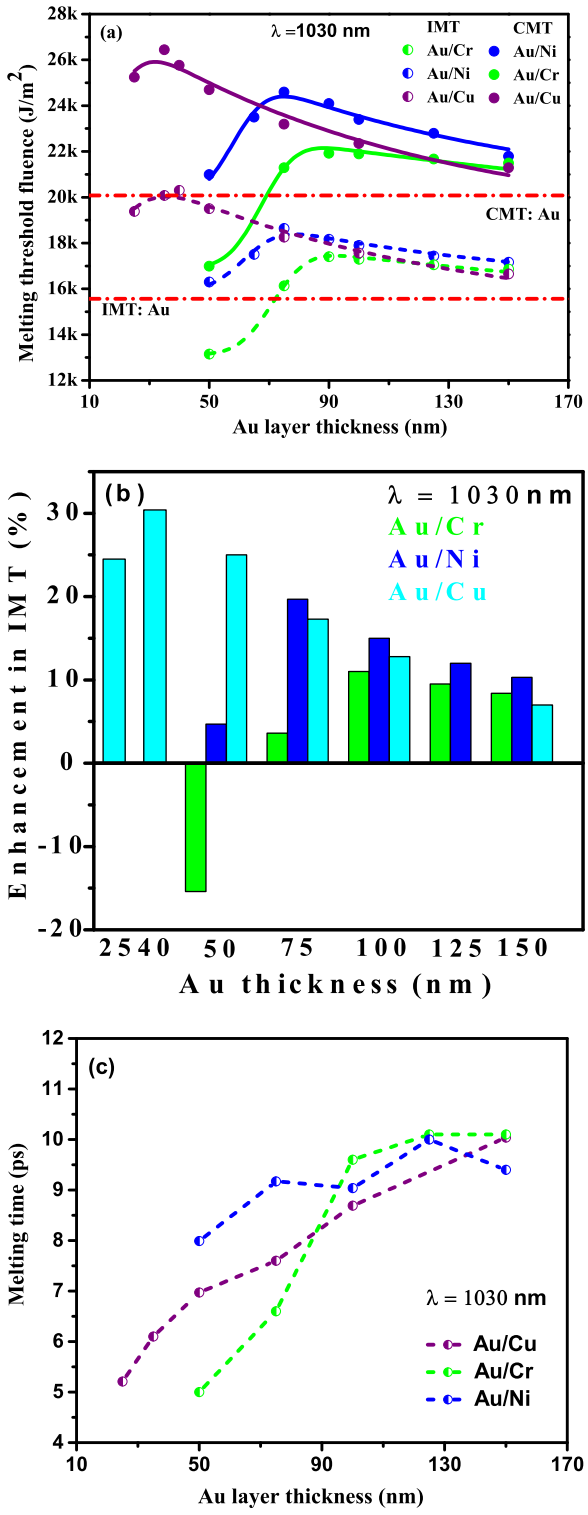

FIG. 6. (a) IMT (half-filled symbols) and CMT (filled symbols) of two-layer Au/M films as a function of Au layer thickness, L_1 for $\lambda = 1030$ nm. Solid and dashed lines refer to fitted curves for CMT and IMT data. (b) Relative enhancement in IMT. (c) Time of melting for varying Au layer thickness of Au/M two-layer films at their respective IMT fluence.

fluence of pure Au at respective wavelengths. The influence of the laser wavelength is to cause a spread of about 5000 K in $T_e^{\max}$ (inset). The rest of the profile is unaffected by laser wavelength.

TABLE III. Derived set of thermophysical parameters for four metals.

Parameter	Au	Ni	Cr	Cu
$T_e^{\max}$ [K]	20000	5000	5000	5000
τ_e [ps]	20.0	7.54	0.92	2.33
τ_l [ps]	39.5	8.87	5.52	21.4
D [$10^{-4}(m^2/s)$]	2.33	0.11	0.98	8.27
L_D [nm]	68.5	9.22	9.47	43.8
ϵ [$10^4 W\sqrt{s}/(m^2\mathrm{K})$]		1.79	0.96	1.39
$\mathcal{E}$ [$J/m^2/\mathrm{K}$]		0.053	0.023	0.064

Figures 7(b) and 7(c) show the effect of different optical absorption on lattice temperature distribution within 200 nm Au/M targets at 10 ps. The figure demonstrates that surface melting of 50 nm Au film can be avoided by embedding it with 150 nm Ni, which itself melts. Further increase of thickness makes Au front surface undergo complete melting and a spatial zone having $T_l = T_M$. Melt-zone width for Au/Ni film is narrower than the pure Au film. Shrinking of the melt zone can be observed for Cr embedding as well. The lowest T_l at the Au surface, observed in the visible range for Au(50)/Ni(150) film, implies the maximum enhancement of melting threshold in this wavelength.

E. Influence of laser wavelength on DT profile of Au/M films

Next, we examine Au thickness dependence of DT for two other wavelengths. Simulated data of IMT (half-filled circles) and CMT (filled circles) as a function of L_1 for Au/Ni (blue) and Au/Cr (green) targets are plotted in Fig. 8. Figures 8(a) and 8(b) represent results of $\lambda = 515$ nm and $\lambda = 343$ nm, respectively. The interesting thing to note is that the IMT/CMT profile for all three wavelengths follow a similar variation with L_1, even though their magnitude differs. To understand the influence of wavelength on DT of Au-based two-layer films, in Fig. 8(c) we have compared the absorbed fluence of IMT for $\lambda = 1030$ nm (circle), 515 nm (rhombus), and 343 nm (square). For Ni and Cr substrates, a constant difference of about 25 J/m^2 between IMT values corresponding to UV and IR lasers can be noticed for L_1 exceeding L_{opt}, where Au undergoes melting. This is in accordance with the difference between IMT of pure Au at these two wavelengths. Optimum Au thickness does not change significantly with laser wavelength although peak absorbed fluence changes (maximum in visible range). IMT of pure Au (horizontal lines shown in the figure) also reflects the same trend. The much higher absorption threshold for Au/Cu film implies that Cu serves as the best substrate material. Performance of Ni and Cr are nearly comparable (Ni offers 4% higher DT at peak).

V. THERMOPHYSICAL ANALYSIS OF DT FOR BIMETALLIC FILMS

Motivated by Ref. [59], we now introduce the derived set of thermophysical parameters that help in analyzing ultrafast

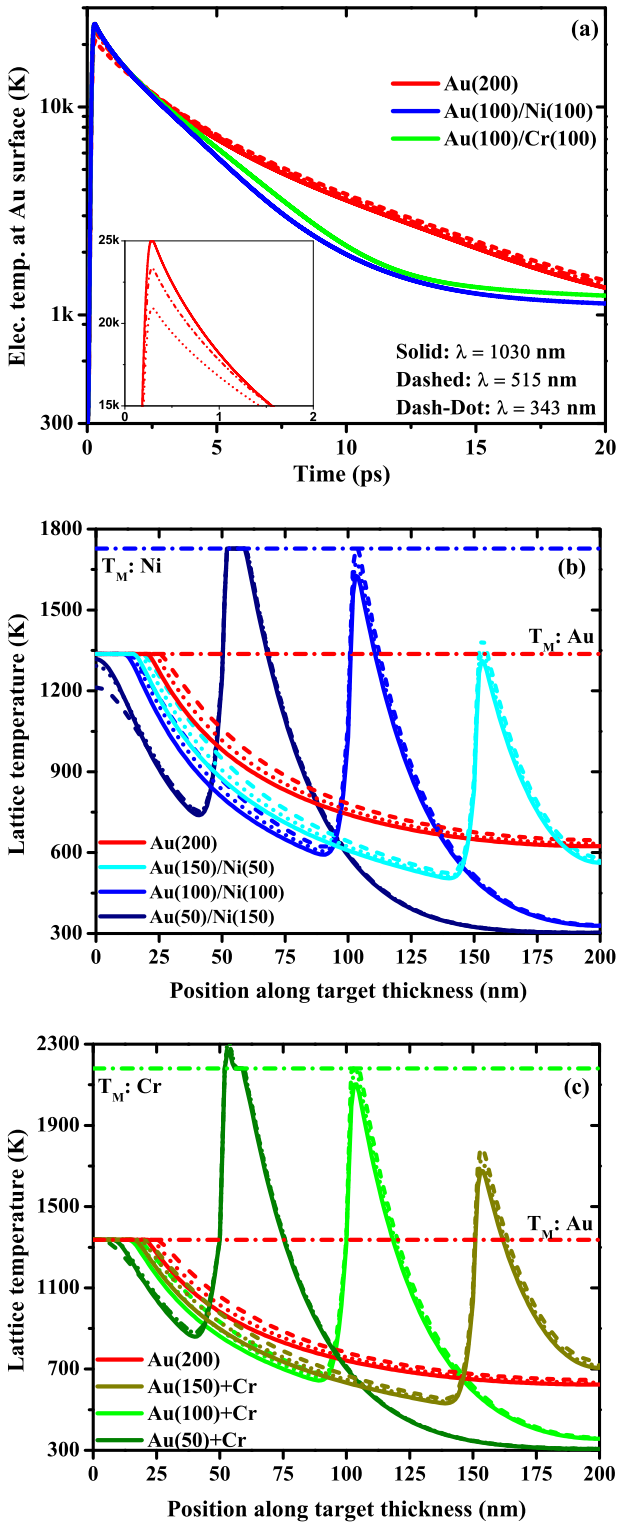

FIG. 7. (a) Time variation of electron temperature at front surface of 200 nm Au film (red), 100/100 Au/Ni (blue), and 100/100 Au/Cr (green) targets. (b) Spatial variation of lattice temperature at 10 ps delay time for 50, 100, and 150 nm Au film and remaining Ni. (c) Same as (b), but for Au/Cr target. Results for IR, visible, and UV lasers are obtained for $I_0 = 20075$ (solid), 990 (dashed), and 588 (dash-dot) J/m^2, i.e., CMT of pure Au at corresponding λ.

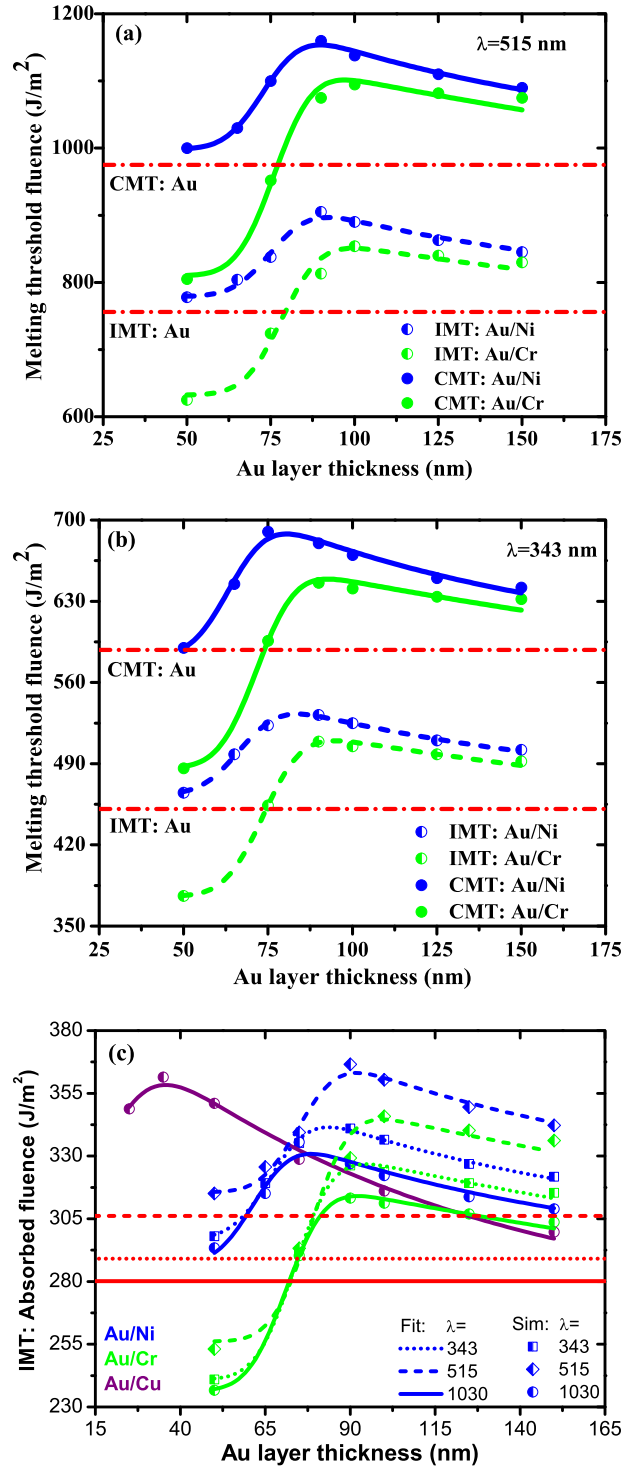

FIG. 8. (a) Melting threshold fluence (incident) of Au/Ni and Au/Cr targets as a function of Au thickness for $\lambda = 515$ nm. (b) Same as (a), but for $\lambda = 343$ nm. Half-filled and filled symbols represent simulation data for IMT and CMT, respectively. Solid and dashed lines refer to fitted curves for CMT and IMT data. (c) Simulation data of IMT (absorbed) and fitted curves are denoted by $\lambda =$ 1030 nm—circle and solid line; 515 nm—rhombus and dashed line; and 343 nm—square and dotted line.

melting of two-layer films and understanding the mechanism of DT enhancement in metal-supported Au film.

First, we introduce characteristic times that play a central role in determining temperature evolution, namely, *electron cooling time*, τ_e and *lattice heating time* τ_l, defined as

$$\tau_e = C_e/G(T) \approx \gamma\left(T_e^{\max} - T_M\right)/G(T),$$
$$\tau_l = C_l/G(T). \tag{11}$$

The above definitions are built under an average approximation wherein we assume that the electron subsystem cools from peak temperature to a value close to melting. More precise quantities would require knowledge of electron and lattice temperature transients describing strong nonequilibrium systems. The beauty of this averaging approximation is that it provides sufficient insights into ultrafast melting of the bilayer system, and predicts optimum interface position and maximum enhancement of DT quite accurately. For illustration, we calculate the characteristic times for melting in pure Au. Following Fig. 4, we consider the maximum electron temperature at the Au surface to be $T_e^{\max} = 20\,000$ K. The actual value will depend on laser fluence under consideration and complete dynamics of temperature evolution. Using the expressions of C_e and $G(T)$ [Eqs. (6) and (8)] in Eq. (11), it turns out that cooling of electrons in Au occurs at about 20 ps, which is much smaller than lattice heating time of about 39.5 ps as shown in Table III.

Figure 4 conveys that depending on the distance from the irradiated surface, the maximum electron temperature at Au/M interface lies in the range of 2000–6000 K. Accordingly, characteristic times for Ni and Cr at a representative electron temperature, $T_e^{\max} = 5000$ K are much lower. Higher values of *e-l* coupling for these two metals are mainly responsible for this. Lower value of τ_l for the chosen substrate metals is exploited in DT enhancement.

Next, we define *electron diffusivity*, an important parameter responsible for electron heat transport, as $D = \kappa_e/C_e$. It is related to the rate at which thermal equilibrium of electron subsystem can be reached. At $T_e^{\max} = 20\,000$ K, our estimate for diffusivity of Au is 2.33 cm^2/s, as given in Table III. It agrees well with the experimental range of 1-3 cm^2/s reported by Block *et al.* [60].

Electron diffusion length, the average distance that excited electrons travel before dissipating their energy through random collisions with electrons and phonons, defined as $L_D = \sqrt{D\tau_e}$ with respect to four metals at representative peak electron temperatures, are shown in Table III. Calculated L_D for Au agrees well with the analytical value obtained by Yang *et al.* [61]. It can be noticed that L_D for Ni and Cr are comparable with their optical penetration depths, whereas in the case of Au and Cu it is much larger than δ.

We also introduce *electron mean-free path* Λ defined as the smallest distance traveled by an electron before changing its energy due to collision. Diffusion length L_D is expressed in terms of Λ as $L_D = \sqrt{1/3\, v_F\, \Lambda\, \tau_e}$, where v_F is the Fermi velocity [48]. The mean-free path could also be calculated using the relation $\Lambda = v_F\, \tau = v_F/(AT_e^2 + BT_l)$, where $\tau = 1/(AT_e^2 + BT_l)$ is the mean collision time.

In the case of USP lasers, absorption of radiation energy by free electrons and subsequent diffusion of hot electrons govern the energy deposition mechanism. If in the path of the hot electrons, another material with higher *e-l* coupling strength is placed, then energy deposition in the second layer causes its lattice subsystem to absorb more energy from the first layer. This causes the second layer to melt at the cost of reduced heating of the lattice subsystem in the first layer. This constitutes the basic principle of melting threshold enhancement by metallic substrate.

To that end, we introduce an *effective electron diffusion length*, L_D^{ef}, of two-layer Au film. It is a measure of the average distance traveled by hot electrons in two different metals in contact before being thermalized to their respective melting temperatures. Consequently, with the observation that at peak DT fluence both metals reach melting, the optimum interface position (L_{opt}) can be linked with the effective electron diffusion length, L_D^{ef}. Depending on the substrate metal, we have two cases of interest. If the electron diffusion length of substrate M is such that $2L_D(M) < L_D(Au)$ as in the case of Ni and Cr, then $L_D^{\text{ef}} \approx L_D(Au) + 2L_D(M)$. For the substrate metal for which $2L_D(M) > L_D(\text{Au})$ (e.g., Cu), we express it as $L_D^{\text{ef}} \approx \delta(\text{Au}) + 2\delta(M)$. L_D^{ef} depends on the time profile of the electron temperature at the front surface of both layers, which eventually depends on parameters of the incident laser as well as the metals involved.

If the interface position is less than the effective diffusion length, then *e-l* thermalization takes place in the second layer. This explains the observed second layer melting for $L_1 < L_{\text{opt}}$. On the other hand, if the interface position lies beyond the effective diffusion length ($L_1 > L_D^{\text{ef}}$), then thermalization of hot electrons occurs in the first layer itself, causing it to melt.

The thermophysical parameter that determines the heat penetration through the interface of two dissimilar materials in contact is *effusivity*, defined as $\epsilon = \sqrt{\kappa_e C_e}$. Since Au is exposed directly to the laser source, its effusion is not important. Numerical values of ϵ for three substrate metals (in contact with Au) corresponding to representative electron temperature $T_e^{\max} = 5000$ K are listed in Table III. Defining *thermal effusion* as $\mathcal{E} = \epsilon\sqrt{\tau_l}$, i.e., heat extraction per unit change in lattice temperature, we observe that this quantity is maximum for Au/Cu and minimum for Au/Cr contacts. The total heat extracted by the substrate to reach its own melting can be estimated by multiplying thermal effusion ($\mathcal{E}$) with lattice temperature difference ΔT_l ($T_M - T_0$). Now, calculating thermal effusion $\mathcal{E}$ at the optimum interface position determined from effective diffusion length for Au/M targets, we find that the total heat extracted by Ni, Cr, and Cu substrates are about 59 J/m^2, 34 J/m^2, and 72 J/m^2, respectively. This extra amount of heat needs to be absorbed by Au from the incident laser to cause melting in both layers. The energy associated with this heat signifies the maximum enhancement in IMT (absorbed fluence) of 200 nm pure Au by introduction of Ni, Cr, and Cu substrates. The robustness of the model is evident from the observation that maximum enhancement in absorbed threshold fluence estimated from thermal effusion agrees with simulated IMT data presented in Fig. 8(c).

VI. ANALYSIS OF DT PROFILE

The distinct profile of IMT/CMT observed in all three substrates corresponding to three different wavelengths as

TABLE IV. Coefficients of fitting function Eq. (12) and other related variables for different Au/M targets at three wavelengths studied here. Units are F_0 in J/m^2; A_r in J/m, $L_0, L_0 + 2\omega$; and L_{opt} in nm. $\omega = 9$ for Au/Ni and Au/Cr; $\omega = 14$ nm (IMT), 10 nm (CMT) for Au/Cu.

Target	DT	F_0	A_r	L_0	$L_0 + 2\omega$	$L_{\text{opt}}^{\text{num}}$
			$\lambda = 343$ nm			
Au/Cr	IMT	375.9	4.3E4	73.8	91.8	94
	CMT	486.3	5.3E4	71.9	89.9	94
Au/Ni	IMT	463.6	8.5E3	67.0	85.0	83
	CMT	582.3	1.3E4	63.9	81.9	83
			$\lambda = 515$ nm			
Au/Cr	IMT	632.3	7.1E4	78.6	96.6	99
	CMT	809.9	9.5E4	76.3	94.3	99
Au/Ni	IMT	779.2	1.4E4	75.4	93.4	92
	CMT	998.4	1.9E4	73.2	91.2	92
			$\lambda = 1030$ nm			
Au/Cr	IMT	13133	1.4E6	71.3	89.3	92
	CMT	16916	1.7E6	67.6	85.6	92
Au/Ni	IMT	15926	3.0E5	62.1	80.1	79
	CMT	19862	5.5E5	58.4	76.4	79
Au/Cu	IMT	14618	7.1E5	14.0	40.0	38
	CMT	18618	9.1E5	14.0	34.0	36

displayed in Figs. 6(a) and 8 motivates us to fit the simulated data with an empirical function that enables better interpretation of the results. The unique function that fits all three cases of bimetallic film is the *exponentially modified Gaussian* function as given below:

$$F_i^{TL}(L_1) = F_0 + \frac{A_r}{L_t}\exp\left[\frac{1}{2}\left(\frac{\omega}{L_t}\right)^2 - \frac{L_1 - L_0}{L_t}\right] \times \int_{-\infty}^{z}\frac{1}{\sqrt{2\pi}}\exp\left[-\frac{y^2}{2}\right]dy; \quad (12)$$

$$z = \frac{L_1 - L_0}{\omega} - \frac{\omega}{L_t}.$$

IMT versus L_1 fitting curves for three different Au/M targets corresponding to three wavelengths are shown by dashed lines of Figs. 6(a) and 8(a)–8(c). The corresponding CMT versus L_1 fittings are shown by solid lines. Excellent agreement of the fitted curves with simulation data (symbols) proves that the proposed analytical function can correctly interpret the observed growth and decay of the melting threshold. With the Gaussian temporal profile of the incident laser and exponential decay of absorbed energy along the target depth, convolution of the two functions in the above form [Eqs. (12)] becomes the natural choice.

Coefficients of the multiparameter fitting are compiled in Table IV. F_0 is the DT offset value referring to the minimum in DT versus L_1 data. A_r is the area under the curve with the base at F_0. Fitting parameters L_0 and ω refer to the mean and standard deviation of the Gaussian function, whereas L_t describes the exponential decay.

Values of L_0 for Au/Ni and Au/Cr cases seen along with data provided in Table III, suggests that it is analogous to the electron diffusion length of pure Au. However, for Au/Cu it is much lower. We can generalize this as $L_0 \approx L_D(\text{Au})$ for a substrate M for which $2L_D(M) < L_D(\text{Au})$ holds. For a substrate metal for which $2L_D(M) > L_D(\text{Au})$ holds, L_0 is equivalent to the optical penetration depth (δ) of Au. Hence, $L_0 = 14$ nm satisfies for all wavelengths in the case of the Au/Cu target.

Fitting parameter ω for both Au/Ni and Au/Cr are found to be about 9 nm and hence fixed at 9 for all wavelengths. Following Table III, this quantity has been associated with the electron diffusion length L_D of Ni and Cr. For the Au/Cu case, fitted values of ω for IMT and CMT are 13 nm and 10 nm, respectively, which is equivalent to the optical penetration depth of Cu.

Finally, L_t refers to the length where the exponential component decays to 36% of its peak value. L_t together with L_0 defines the length beyond which the correlation between the two functions becomes negligible. Irrespective of wavelength, a substrate specific value of $L_t = 100$ nm for Au/Ni, Au/Cu films and 300 nm for Au/Cr has served the best purpose. This is in consonance of the observation that for $L_1 > L_0 + L_t$ ($\approx$ 175 nm for Ni, 115 nm for Cu), the second layer does not significantly influence the DT. A higher value of L_t in Cr indicates slower decay of DT in Au/Cr film beyond $L_1 = 400$ nm.

The optimum Au thickness (L_{opt}) for which IMT/CMT is maximum has been obtained by carrying out the numerical differentiation of F_i^{TL} with respect to L_1 and equating it to zero. From Table IV, it is quite apparent that L_{opt} for all the substrates follow a unique relation: $L_{\text{opt}} \approx L_0 + 2\omega \approx L_D^{\text{ef}}$, within a spread of $\approx$ 4%. Hence the optimum thickness of the first layer (Au) for maximizing the DT of Au/M film is related to the effective electron diffusion length of the two-layer target. This reinforces our analysis on bimetallic films using the assumed functional form of DT. It can be observed that the position of maximum does not vary significantly with wavelength. Moreover, maximum enhancement in absorbed fluence supports the values calculated from the total heat extracted from Au by the second layer due to thermal effusion.

We emphasize that the proposed function is able to predict both quantities of interest in the context of DT enhancement, i.e., the optimum interface position and the maximum realizable enhancement offered by any substrate quite satisfactorily. Success of this function in describing the DT profile, (independently for IMT and CMT) with remarkable accuracy for wide range of wavelengths makes it ubiquitous. Consistent interpretation of fitting coefficients with thermophysical parameters of bimetallic film makes the model robust.

Incidentally, melting of the Cu layer for $L_1 < 38$ nm (L_{opt}) for Au/Cu film is in agreement with the TTM-MD-based simulation of Ref. [62] that reported preferential subsurface melting of the Cu substrate, while overlaying 30 nm Au film largely retained its original crystalline structure.

VII. CONCLUSIONS

We report development of Python-based TTM code for the study of fs laser heating and associated thermal damage of bimetallic films. Two different concepts of laser-induced DT, viz. incipient melting threshold: IMT and complete melting threshold: CMT, are implemented in the code. IMT and CMT of 200 nm Au/M (M = Ni, Cr, Cu) films are determined for increasing thickness of the Au layer. Results for three different

wavelengths of a 100 fs laser are compared to demonstrate the influence of different substrate metals in enhancing ultrafast melting threshold. Important conclusions arising from our study are summarized below.

(1) Our paper reveals that for every substrate metal, there exists an optimum thickness of the Au layer (lowest for Cu and highest for Cr) that offers maximum enhancement of DT. Cu substrate also offers maximum enhancement.

(2) DT enhancement of bimetallic films is analyzed through a derived set of thermophysical parameters, e.g., electron cooling time, lattice heating time, diffusivity, and effusivity of electrons.

(3) Optimum interface position and maximum enhancement in DT are quantified from effective electron diffusion length of two-layer films and total extracted heat through contact surface due to thermal effusion.

(4) A unique analytical function is proposed to express DT profile of two-layer films. The proposed function explains the observed peaking in DT at certain thickness of Au layer. This constitutes one of the main achievements of the present theoretical paper. Ubiquitousness of the function is reflected by successful application in explaining DT profile for three different substrate metals and three different wavelengths.

(5) The robustness of the proposed analytical function is ascertained by associating all the coefficients with the derived set of thermophysical parameters of the layer materials. Additionally, maximum enhancement in DT and position of the maximum arising from the analytical function are in excellent agreement with those obtained from thermophysical analysis.

(6) The current paper establishes a comprehensive theoretical model for fs laser-induced damage with respect to incipient and complete melting of Au film embedded on different elemental metals.

(7) Finally, ideas put forward here could help in predicting DT of any arbitrary substrate material, provided their thermophysical parameters are known.

[1] E. G. Gamaly, *Femtosecond Laser-Matter Interaction: Theory, Experiments and Applications* (CRC Press, Taylor & Francis Group, Boca Raton, 2011).

[2] G. Ausanio, S. Amoruso, A. C. Barone, R. Bruzzese, V. Iannotti, L. Lanotte, and M. Vitiello, Production of nanoparticles of different materials by means of ultrashort laser pulses, Appl. Surf. Sci. **252**, 4678 (2006).

[3] M. N. Ashfold, F. Claeyssens, G. M. Fuge, and S. J. Henley, Pulsed laser ablation and deposition of thin films, Chem. Soc. Rev. **33**, 23 (2004).

[4] M. Maiuri, M. Garavelli, and G. Cerullo, Ultrafast spectroscopy: State of the art and open challenges, J. Am. Chem. Soc. **142**, 3 (2020).

[5] R. Ernstorfer, M. Harb, C. T. Hebeisen, G. Sciaini, T. Dartigalongue, and R. D. Miller, The formation of warm dense matter: Experimental evidence for electronic bond hardening in gold, Science **323**, 1033 (2009).

[6] B. C. Stuart, M. D. Feit, S. Herman, A. M. Rubenchik, B. W. Shore, and M. D. Perry, Optical ablation by high-power short-pulse lasers, J. Opt. Soc. Am. B **13**, 459 (1996).

[7] J. Güdde, J. Hohlfeld, J. G. Müller, and E. Matthias, Damage threshold dependence on electron-phonon coupling in Au and Ni films, Appl. Surf. Sci. **127-129**, 40 (1998).

[8] S.-S. Wellershoff, J. Hohlfeld, J. Güdde, and E. Matthias, The role of electron-phonon coupling in femtosecond laser damage of metals, Appl. Phys. A **69**[Suppl.], S99 (1999).

[9] J. Krüger, D. Dufft, R. Koter, and A. Hertwig, Temperature dependences of the electron-phonon coupling, electron heat capacity and thermal conductivity in Ni under femtosecond laser irradiation, Appl. Surf. Sci. **253**, 7815 (2007).

[10] B. S. Yilbas, Short-pulse laser heating of gold–chromium layers: Thermo-elasto-plastic analysis, J. Phys. D: Appl. Phys. **35**, 1210 (2002).

[11] T. Q. Qiu and C. L. Tien, Femtosecond laser heating of multi-layer metals—I. Analysis, Int. J. Heat Mass Transf. **37**, 2789 (1994).

[12] T. Q. Qiu, T. Juhasz, C. Suarez, W. E. Bron, and C. L. Tien, Femtosecond laser heating of multi-layer metals—II. Experiments, Int. J. Heat Mass Transf. **37**, 2799 (1994).

[13] B. Wang and L. Gallais, A theoretical investigation of the laser damage threshold of metal multi-dielectric mirrors for high power ultrashort applications, Opt. Express **21**, 14698 (2013).

[14] G. Du, Q. Yang, F. Chen, Y. Wu, Y. Ou, Y. Lu, and X. Hou, Ultrafast thermalization dynamics in two-layer metal films excited by temporally shaped femtosecond laser, Int. J. Heat Mass Transf. **87**, 341 (2015).

[15] A. Bora, W. Dai, J. P. Wilson, and J. C. Boyt, Neural network method for solving parabolic two-temperature microscale heat conduction in double-layered thin films exposed to ultrashort-pulsed lasers, Int. J. Heat Mass Transf. **178**, 121616 (2021).

[16] K. Hlinomaz, Y. Levy, T. J.-Y. Derrien, and N. M. Bulgakova, Modeling thermal response of Mo thin films upon single femtosecond laser irradiation: Dynamics of film melting and substrate softening, Int. J. Heat Mass Transf. **196**, 123292 (2022).

[17] T. Okada, T. Tomita, H. Katayama, Y. Fuchikami, T. Ueki, H. Hisazawa, and Y. Tanaka, Local melting of Au/Ni thin films irradiated by femtosecond laser through GaN, Appl. Phys. A **125**, 690 (2019).

[18] B. Gaković, P. A. Danilov, S. I. Kudryashov, D. Milovanović, A. Radulović, P. Panjan, and A. A. Ioni, The morphological and compositional changes of bimetallic Ti/Al thin film induced by ultra-short laser pulses, Eur. Phys. J. D **75**, 288 (2021).

[19] W. M. G. Ibrahim, H. E. Elsayed-Ali, C. E. Bonner Jr., and M. Shinn, Ultrafast investigation of electron dynamics in multilayer metals, Int. J. Heat Mass Transf. **47**, 2261 (2004).

[20] A. M. Chen, H. F. Xu, Y. F. Jiang, L. Z. Sui, D. J. Ding, H. Liu, and M. X. Jin, Modeling of femtosecond laser damage threshold on the two-layer metal films, Appl. Surf. Sci. **257**, 1678 (2010).

[21] A. Suslova and A. Hassanein, Femtosecond laser absorption, heat propagation, and damage threshold analysis for Au coating on metallic substrates, Appl. Surf. Sci. **422**, 295 (2017).

[22] S. I. Anisimov, B. L. Kapeliovich, and T. L. Perel'Man, Electron emission from metal surfaces exposed to ultrashort laser pulses, Sov. Phys.-JET **39**, 375 (1974).

[23] C. W. Cheng, S. Y. Wang, K. P. Chang, and J. K. Chen, Femtosecond laser ablation of copper at high laser influence: Modeling and experimental comparison, Appl. Surf. Sci. **361**, 41 (2016).

[24] J. Zhang, Y. Chen, M. Hu, and X. Chen, An improved three-dimensional two-temperature model for multi-pulse femtosecond laser ablation of aluminum, J. Appl. Phys. **117**, 063104 (2015).

[25] X. Jia and X. Zhao, Numerical study of material decomposition in ultrafast laser interaction with metals, Appl. Surf. Sci. **463**, 781 (2019).

[26] P. Bresson, J.-F. Bryche, M. Besbes, J. Moreau, P.-L. Karsenti, P. G. Charette, D. Morris, and M. Canva, Improved two-temperature modeling of ultrafast thermal and optical phenomena in continuous and nanostructured metal films, Phys. Rev. B **102**, 155127 (2020).

[27] J. K. Chen, D. Y. Tzou, and J. E. Beraun, A semiclassical two-temperature model for ultrafast laser heating, Int. J. Heat Mass Transf. **49**, 307 (2006).

[28] P. B. Corkum, F. Brunel, N. K. Sherman, and T. Srinivasan-Rao, Thermal Responses of Metals to Ultrashort-Pulse Laser Excitation, Phys. Rev. Lett. **61**, 2886 (1988).

[29] A. Suslova and A. Hassanein, Numerical simulation of ballistic electron dynamics and heat transport in metallic targets exposed to ultrashort laser pulse, J. Appl. Phys. **124**, 065108 (2018).

[30] E. Carpene, Ultrafast laser irradiation of metals: Beyond the two-temperature model, Phys. Rev. B **74**, 024301 (2006).

[31] L. Jiang and H. Tsai, Improved two-temperature model and its application in ultrashort laser heating of metal films, J. Heat Transfer **127**, 1167 (2005).

[32] L. Waldecker, R. Bertoni, and R. Ernstorfer, Electron-Phonon Coupling and Energy Flow in a Simple Metal Beyond the Two-Temperature Approximation, Phys. Rev. X **6**, 021003 (2016).

[33] F. Akhmetov, N. Medvedev, I. Makhotkin, M. Ackermann, and I. Milov, Electron–phonon coupling in two-temperature model, Materials **15**, 5193 (2022).

[34] X. Zhao and Y. C. Shin, Femtosecond laser ablation of aluminum in vacuum and air at high laser intensity, Appl. Surf. Sci. **283**, 94 (2013).

[35] J. P. Colombier, P. Combis, F. Bonneau, R. Le Harzic, and E. Audouard, Hydrodynamic simulations of metal ablation by femtosecond laser irradiation, Phys. Rev. B **71**, 165406 (2005).

[36] M. E. Povarnitsyn, T. E. Itina, M. Sentis, K. V. Khishchenko, and P. R. Levashov, Material decomposition mechanisms in femtosecond laser interactions with metals, Phys. Rev. B **75**, 235414 (2007).

[37] M. E. Povarnitsyn, V. B. Fokin, and P. R. Levashov, Microscopic and macroscopic modelling of femtosecond laser ablation of metals, Appl. Surf. Sci. **357**, 1150 (2015).

[38] F. Caruso and D. Novko, Ultrafast dynamics of electrons and phonons: From the two temperature model to the time-dependent Boltzmann equation, Adv. Phys. X **7**, 2095925 (2022).

[39] D. Perez and L. J. Lewis, Molecular-dynamics study of ablation of solids under femtosecond laser pulses, Phys. Rev. B **67**, 184102 (2003).

[40] L. V. Zhigilei, Z. Lin, and D. S. Ivanov, Atomistic modeling of short pulse laser ablation of metals: Connections between melting, spallation, and phase explosion, J. Phys. Chem. C **113**, 11892 (2009).

[41] M. E. Povarnitsyn, V. B. Fokin, and P. R. Levashov, and T. E. Itina, Molecular dynamics simulation of subpicosecond double-pulse laser ablation of metals, Phys. Rev. B **92**, 174104 (2015).

[42] N. N. Nedialkov, P. A. Atanasov, S. Amoruso, R. Bruzzese, and X. Wang, Laser ablation of metals by femtosecond pulses: Theoretical and experimental study, Appl. Surf. Sci. **253**, 7761 (2007).

[43] N. Tsakiris, K. K. Anoop, G. Ausanio, M. Gill-Comeau, R. Bruzzese, S. Amoruso, and L. J. Lewis, Ultrashort laser ablation of bulk copper targets: Dynamics and size distribution of the generated nanoparticles, J. Appl. Phys. **115**, 243301 (2014).

[44] D. Ivanov and L. V. Zhigilei, Combined atomistic-continuum modeling of short-pulse laser melting and disintegration of metal films, Phys. Rev. B **68**, 064114 (2003).

[45] Y. Li, Y. Li, L. Feng, and G. Lu, Metal alloy nanowire joining induced by femtosecond laser heating: A hybrid atomistic-continuum interpretation, Int. J. Heat Mass Transf. **150**, 119287 (2020).

[46] A. M. Prokhorov, V. I. Konov, I. Ursu, and I. N. Mihailescu, *Laser Heating of Metals* (CRC Press, Taylor & Francis Group, Boca Raton, 1990).

[47] P. G. Etchegoin, E. C. Le Ru, and M. Meyer, An analytical model for the optical properties of gold, J. Chem. Phys. **125**, 164705 (2006).

[48] C. Kittel, *Introduction to Solid State Physics* (Wiley, New York, 1976).

[49] R. H. M. Groeneveld, R. Sprik, and A. Lagendijk, Femtosecond spectroscopy of electron-electron and electron-phonon energy relaxation in Ag and Au, Phys. Rev. B **51**, 11433 (1995).

[50] X. Wang, D. Riffe, Y. Lee, and M. Downer, Time-resolved electron-temperature measurement in a highly excited gold target using femtosecond thermionic emission, Phys. Rev. B **50**, 8016 (1994).

[51] B. Christensen, K. Vestentoft, and P. Balling, Short-pulse ablation rates and the two-temperature model, Appl. Surf. Sci. **253**, 6347 (2007).

[52] Z. Lin and L. V. Zhigilei, Temperature dependence of the electron–phonon coupling, electron heat capacity and thermal conductivity in Ni under femtosecond laser irradiation, Appl. Surf. Sci. **253**, 6295 (2007).

[53] C. D. Aeaby and A. Ray, Femtosecond Laser Induced Heat Propagation and Damage Threshold Analysis of Au/Cr Two-Layer Film (DAE-BRNS National Laser Symposium, CP-06-03, NLS-1044, 2022), https://www.nls30.com.

[54] R. P. Fedkiw, T. Aslam, B. Merriman, and S. Osher, A non-oscillatory Eulerian approach to interfaces in multimaterial flows (the ghost fluid method), J. Comput. Phys. **152**, 457 (1999).

[55] E. L. Gurevich, Y. Levy, S. V. Gurevich, and N. M. Bulgakova, Role of the temperature dynamics in formation of nanopatterns upon single femtosecond laser pulses on gold, Phys. Rev. B **95**, 054305 (2017).

[56] M. K. El-Adawi, M. A. Abdel-Naby, and S. A. Shalaby, Laser heating of a two-layer system with constant surface absorption: An exact solution, Int. J. Heat Mass Transf. **38**, 947 (1995).

[57] J. K. Chen and J. E. Beraun, Modelling of ultrashort laser ablation of gold films in vacuum, J. Opt. A: Pure Appl. Opt. **5**, 168 (2003).

[58] S. Noël, J. Hermann, and T. Itina, Investigation of nanoparticle generation during femtosecond laser ablation of metals, Appl. Surf. Sci. **253**, 6310 (2007).

[59] S. Nolte, C. Momma, H. Jacobs, A. Tunnermann, B. N. Chichkov, B. Wellegehausen, and H. Welling, Ablation of metals by ultrashort laser pulses, J. Opt. Soc. Am. B **14**, 2716 (1997).

[60] A. Block, M. Liebel, R. Yu, M. Spector, Y. Sivan, F. J. García de Abajo, and N. F. van Hulst, Tracking ultrafast hot-electron diffusion in space and time by ultrafast thermomodulation microscopy, Sci. Adv. **5**, eaav8965 (2019).

[61] J. Yang, Y. Zhao, and X. Zhu, Theoretical studies of ultrafast ablation of metal targets dominated by phase explosion, Appl. Phys. A **89**, 571 (2007).

[62] D. A. Thomas, Z. Lin, L. V. Zhigilei, E. L. Gurevich, S. Kittel, and R. Hergenröder, Atomistic modeling of femtosecond laser-induced melting and atomic mixing in Au film–Cu substrate system, Appl. Surf. Sci. **255**, 9605 (2009).